23rd Australasian Fluid Mechanics Conference - 23AFMC
Sydney, Australia
4 – 8 December 2022

Paper No: AFMC2022-255

Scaling of Microbubble Generation in a T-junction

Aaron Ailwood[1], **James A. Venning**[1*], **Luka Barbaca**[1], **Patrick S. Russell**[1], **Bryce W. Pearce**[1] **and Paul A. Brandner**[1]

[1] Cavitation Research Laboratory, Australian Maritime College, University of Tasmania, Launceston, TAS 7250
*mailto: james.venning@utas.edu.au

Abstract

Microbubble generation in a microfluidic T-junction was investigated in the context of artificial nuclei seeding of hydrodynamic facilities. Microbubble size distribution and production rate were investigated for a range of air, water and outlet pressures using high-speed shadowgraphy. The generator was found to produce a train of monodisperse bubbles approximately 100 μm in diameter across a range of operating conditions. The only exception to this being the cases with a large difference between the air and water supply pressures where bubble coalescence was prominent. An empirical scaling law depicting the dependence of bubble diameter on the operational conditions was developed by fitting all the data using least-squares regression. Bubble production frequency was found to exhibit a quadratic increase with an increase in the difference between the air supply and the outlet pressure. Production frequencies in the range 0 kHz to 3.5 kHz were observed across the range of investigated conditions. The reported work demonstrates the T-junction to be a robust device for monodisperse microbubble generation and a useful tool for experimental modelling of nucleation effects in hydrodynamic facilities.

1 Introduction

Microbubbles, i.e. bubbles smaller than 1 mm in diameter, are a topic of interest in a wide variety of applications ranging from medicine, pharmacology, material science to food industry (Rodriguez-Rodriguez *et al.*, 2015). In hydrodynamic applications, the presence of microbubbles within a fluid alters its mechanical properties, particularly its susceptibility to cavitation. Pure water can withstand considerable tension (Temperley and Chambers, 1946), although in practical flows, water contains sites of weakness, and it is at these local inhomogeneities that cavitation inception occurs. These may be microbubbles, organisms, or unwetted solids, and are termed 'cavitation nuclei'. Recent model scale studies have shown that the water nuclei population alters the critical cavitation number (Khoo *et al.*, 2021), the nature and dynamics of cavitation (Brandner *et al.*, 2022), the unsteady loads (Venning *et al.*, 2022) and generation of microbubbles from cavitation (Russell *et al.*, 2018a).

The disparate requirements of different microbubble applications have led to development of various methods for microbubble generation. Microfluidic devices are utilised in applications where monodisperse bubbles, i.e. bubbles of the same size, are required (Anna *et al.*, 2016). Alternatively, polydisperse populations, with bubbles of various sizes, can be generated via rapid depressurisation of supersaturated water through an orifice (e.g. Barbaca *et al.*, 2020).

At the University of Tasmania Cavitation Research Laboratory (CRL), monodisperse bubbles approximately 100 μm in diameter are used for artificial nuclei seeding. Monodisperse bubble populations are routinely generated using commercial microfluidic T-junction devices developed by YLec Consultants (Russell *et al.*, 2018b). Analytical models for microbubble production are usually difficult to obtain due to the complexity of the flow in terms of compressibility, small length scales, and complex interfacial interactions. As such, experimental data is necessary to relate the input parameters of a microbubble generator to its production performance. While, abundant literature on bubble generation in microfluidic devices exists, the majority of reported studies either consider use of surfactants to stabilise the bubble train, or generation of bubbles that are too large to be used as cavitation nuclei. In addition, many of the models characterising the bubble production are developed for different microfluidic device geometries, e.g. flow focusing or rectangular cross-sections. The scope of the current work is to report a comprehensive study of bubble generation from a non-degrading device suitable for artificial nuclei seeding .

2 Methods

The experiments were performed at the AMC CRL using a custom designed experimental apparatus for evaluating microbubble generators. The apparatus consists of a T-junction device with the outlet incorporated into a pressure chamber, and pressurised water and air supply systems. A schematic of the experimental apparatus is presented in figure 1.

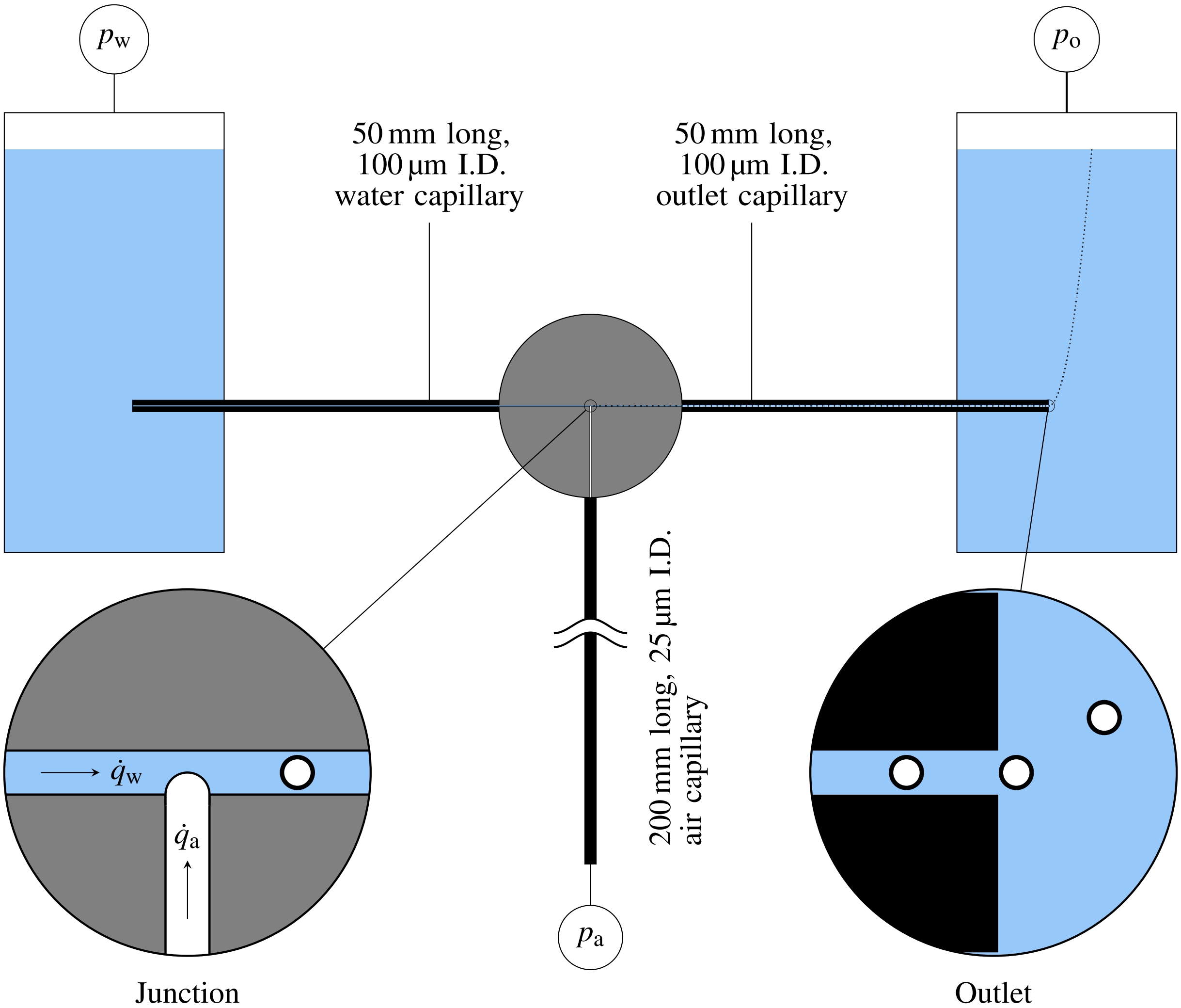

Figure 1: A schematic of the experimental apparatus used for characterisation of bubble production from a T-junction generator. The water is supplied to the junction from pressurised water canister through a capillary tube. Another capillary tube is utilised to deliver pressurised air. The outlet of the T-junction discharges into a pressure chamber (right inset). The left inset is an enlarged representation of the flow at the junction.

Microbubbles are generated using a 100 µm bore stainless steel T-junction, custom produced for AMC by Valco Inc. The two inlets of the T-junction are connected to the water and air supply. The water is supplied to the T-junction from a pressurised canister with an air-water interface through a 100 μm diameter, 50 mm long capillary tube. The water pressure, p_w, is controlled via a ProportionAir QPV series electronic regulator (range 0 bar to 10 bar absolute). Pressurised air is delivered to the T-junction via a 25 μm diameter, 200 mm long capillary tube, with the supply pressure, p_a, regulated using an identical regulator as that used for the water supply, additionally equipped with a Prevost 1 μm air filter. A 100 μm diameter, 50 mm long capillary tube was connected to the T-junction outlet, and was used to deliver the bubble-laden flow to the pressure chamber. The outlet pressure, p_o, was controlled via pressure feedback, a PI control loop and two control valves connected to high- and low-pressure sources. The range of p_o values was in range 50 kPa to 200 kPa.

The microbubble size and production rate were analysed using high-speed shadowgraphy from a Phantom v2640 high-speed camera (maximum resolution of 2048 × 1920 pixels) equipped with an InfiniProbe TS-160 microscope. This optical setup resulted with a spatial resolution of 0.26 pixel/μm. Telecentric back-light was supplied by a 45 mm diameter Effilux Effi-Tele-45-000 LED projector. Sample photographs obtained using this system are shown in figure 2.

For each data point, the measurements were performed by first setting p_o, followed by p_w and p_a. A sequence of 5000 frames was acquired at a frame rate of 24,000 frames per second, corresponding to 0.2 s time period. The images were processed using MATLAB and LaVision DaVis to extract the microbubble size and the production rate. In order to alleviate the issues of bubble coalescence in the quiescent chamber volume, as well as to avoid the optical imperfections near the image edges, image processing was only performed for the region 0.4 mm downstream of the outlet tube. Note that the vertical acceleration of the bubble train seen on the right side of figure 2 is due to the buoyancy of larger coalesced bubbles.

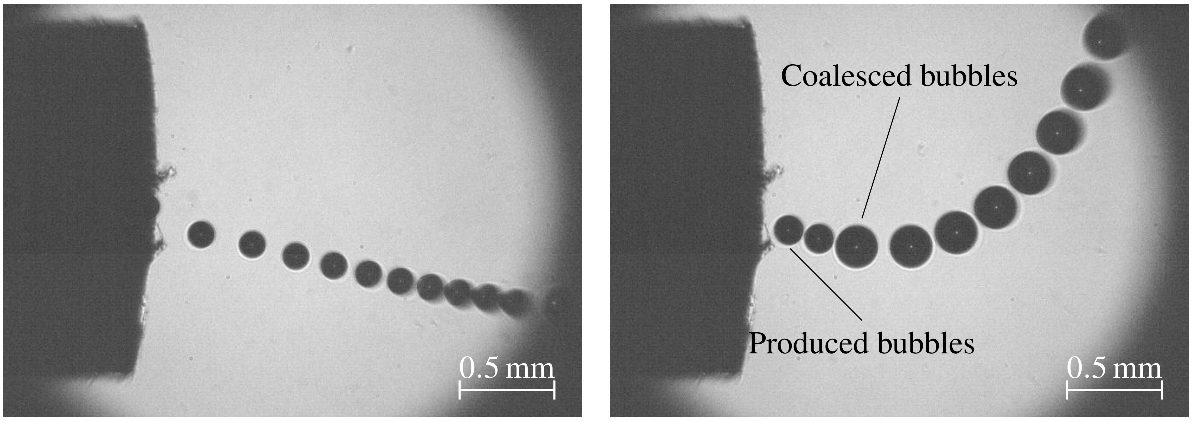

Figure 2: Photographs of microbubbles exiting the outlet tube. The left image represents the conditions where a monodisperse bubble train is produced. The right photograph shows coalescing bubbles.

3 Results

The initial discussion is focused on the cases where the outlet pressure was held constant ($p_o = 100$ kPa), while p_w and p_a were varied. A map of the dependence of the mean microbubble diameter (d) on air and water pressures is given in figure 3. For presentation purposes, the pressure difference between the water supply and outlet pressures, $p_w - p_o$, termed 'driving pressure', is utilised. For a constant $p_w - p_o$, an increase in p_a leads to an increase in d. The rate of increase in bubble diameter appears to be larger at lower $p_w - p_o$ values. The generation of microbubbles larger than the internal diameter of the outlet tube (100 μm) for the majority of cases indicates formation of a slug flow within the capillary. The slug flow may lead to bubble coalescence in the outlet tube and may explain the observed increase in d at lower $p_w - p_o$ values.

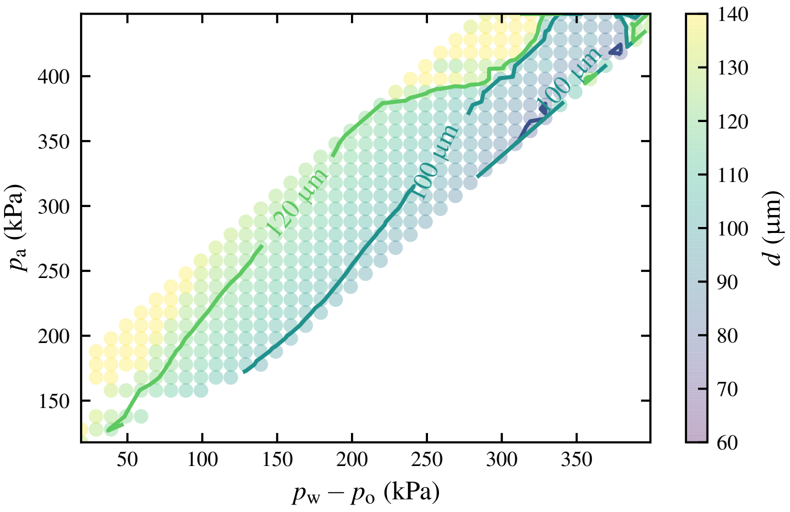

Figure 3: Diameter of generated microbubbles as a function of the driving pressure difference ($p_w - p_o$) and the air pressure (p_a), for a constant outlet pressure, $p_o = 100$ kPa.

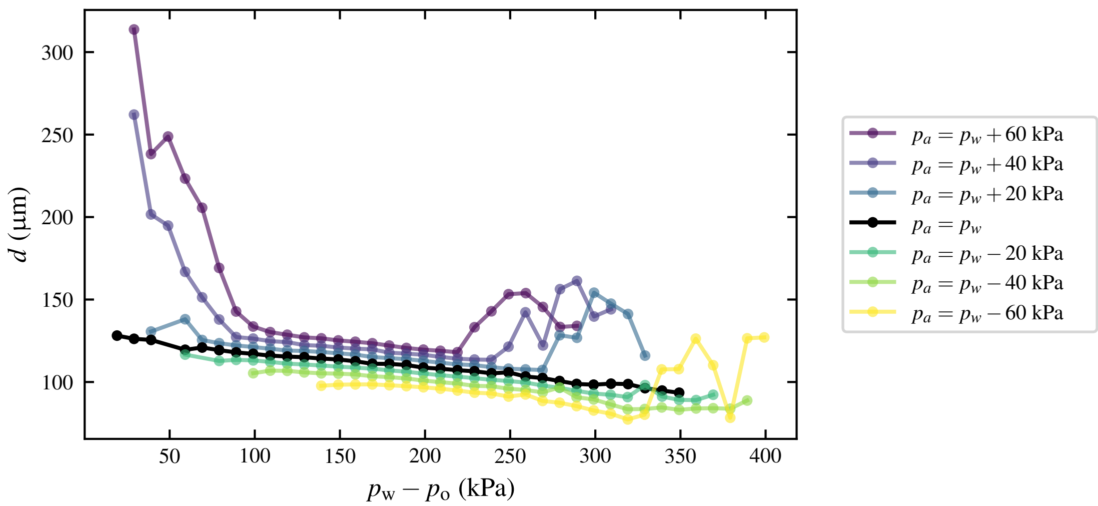

Figure 4: Microbubble diameter as a function of driving pressure difference for each combination of air and water pressures, for a constant outlet pressure $p_o = 100$ kPa.

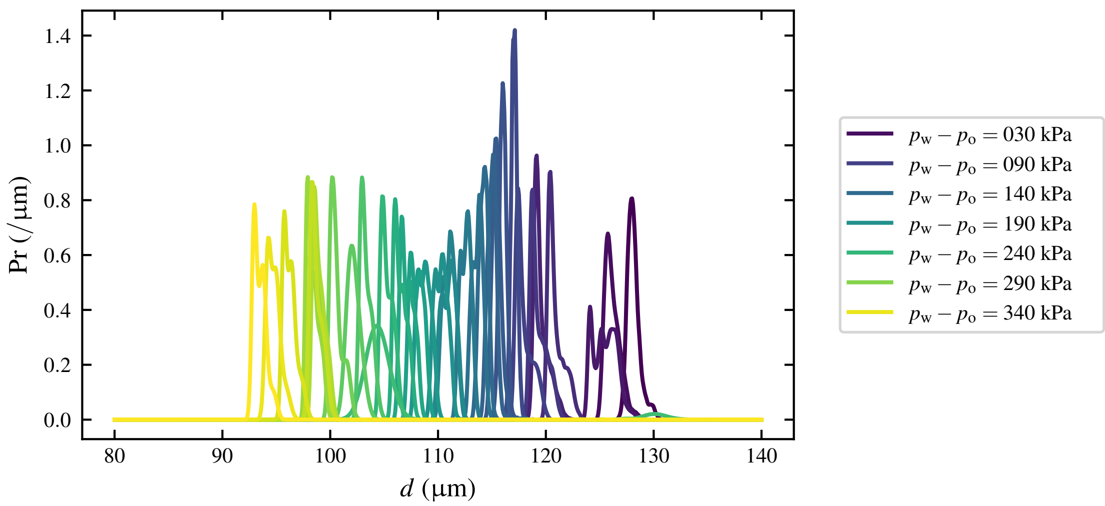

Figure 5: Microbubble size distribution expressed as a probability density function of d for cases with $p_a = p_w$ and a constant outlet pressure, $p_o = 100$ kPa.

Further insight into the microbubble diameter behaviour can be gained if the map presented in figure 3 is re-plotted as a series of curves with a constant differential between the air and water supply pressures, $p_a - p_w$. This data is presented in figure 4. For the conditions where $p_a = p_w$ (black), a monodisperse bubble train is observed across the whole range of driving pressures, with a slight decrease in d observed with an increase in $p_w - p_o$. Following an increase in $p_a - p_w$, the mean diameter of generated microbubbles increases. At the extremes of operation, the bubble train becomes more susceptible to coalescence, and this is reflected through a large increase in d.

Microbubble size distributions for the cases with $p_w = p_a$, i.e. corresponding to the black points in figure 4, are shown in figure 5. These were estimated using the kernel density estimation with a Gaussian kernel, with the estimator bandwidth determined using Scott's rule (Scott, 2015). All the distributions are monodisperse, with a typical spread in d value of the order of a few micrometers. The standard deviation of the bubble diameters is typically ≈ 0.5 µm.

The microbubble production rate, f, was determined from high-speed videos by analysing the intensity of a vertical line of pixels located just downstream of the outlet tube. As the production rate is postulated to depend on the flow rate of air ($\dot{q}_a$), in figure 6 f is plotted as a function of pressure differential between the air supply and the outlet, $p_a - p_o$. Each curve represents the dependence of f on $p_a - p_o$ for a constant $p_a - p_w$. Along each curve, f increases with p_a. The production frequency was observed to increase with a square of the pressure difference $p_a - p_o$, apart from the cases at the extremes of the pressure difference, where the generator operation becomes unstable. A variation in the curve gradient for different $p_a - p_w$ may be attributed to the change in d, i.e. for a given $p_a - p_o$, a lower p_w results with larger bubbles and thus a lower f for the same $\dot{q}_a$.

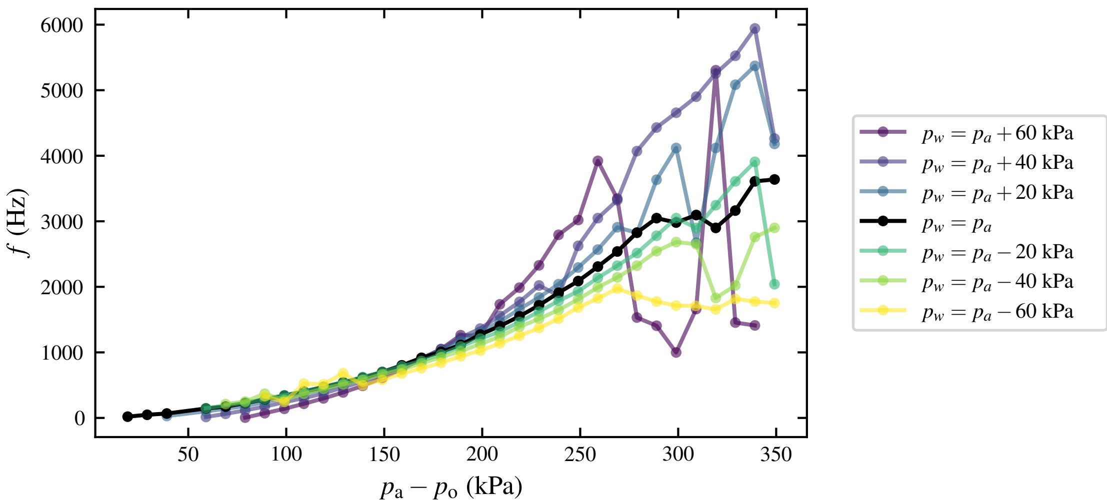

Figure 6: Production rate f as a function of the air to outlet pressure difference ($p_a - p_o$) for each combination of air and water pressures and a constant outlet pressure ($p_o = 100$ kPa)

.

Maps of dependence of d on $p_w - p_o$ across a range of investigated p_o values are given in figure 7. The trends in d behaviour, discussed above for $p_o = 100$ kPa, remain pertinent for all p_o values, however it can be seen that for a given p_a and $p_w - p_o$ combination, d decreases with an increase in p_o.

The d datasets corresponding to the conditions where $p_a = p_w$ across the range of investigated p_o values are presented in figure 8. Regardless of p_o value, monodisperse bubble trains are observed across the whole range of the investigated $p_w - p_o$ values. In all cases, d decreases with an increase in $p_w - p_o$, with the rate of decreases relatively similar for all p_o values. It is worth noting that that the diameter data are not monotonic with p_o. This may be attributed to the temporal order of the testing, and a possible contamination of the generator during prolonged tests. For practical nucleation purposes, the strengths of generated microbubbles, i.e. the tension required for activation, are similar and close to the water vapour saturation pressure. Given that the bubble train remains monodisperse, even when contamination is present, the effect of contamination on the T-junction device operation is not deemed

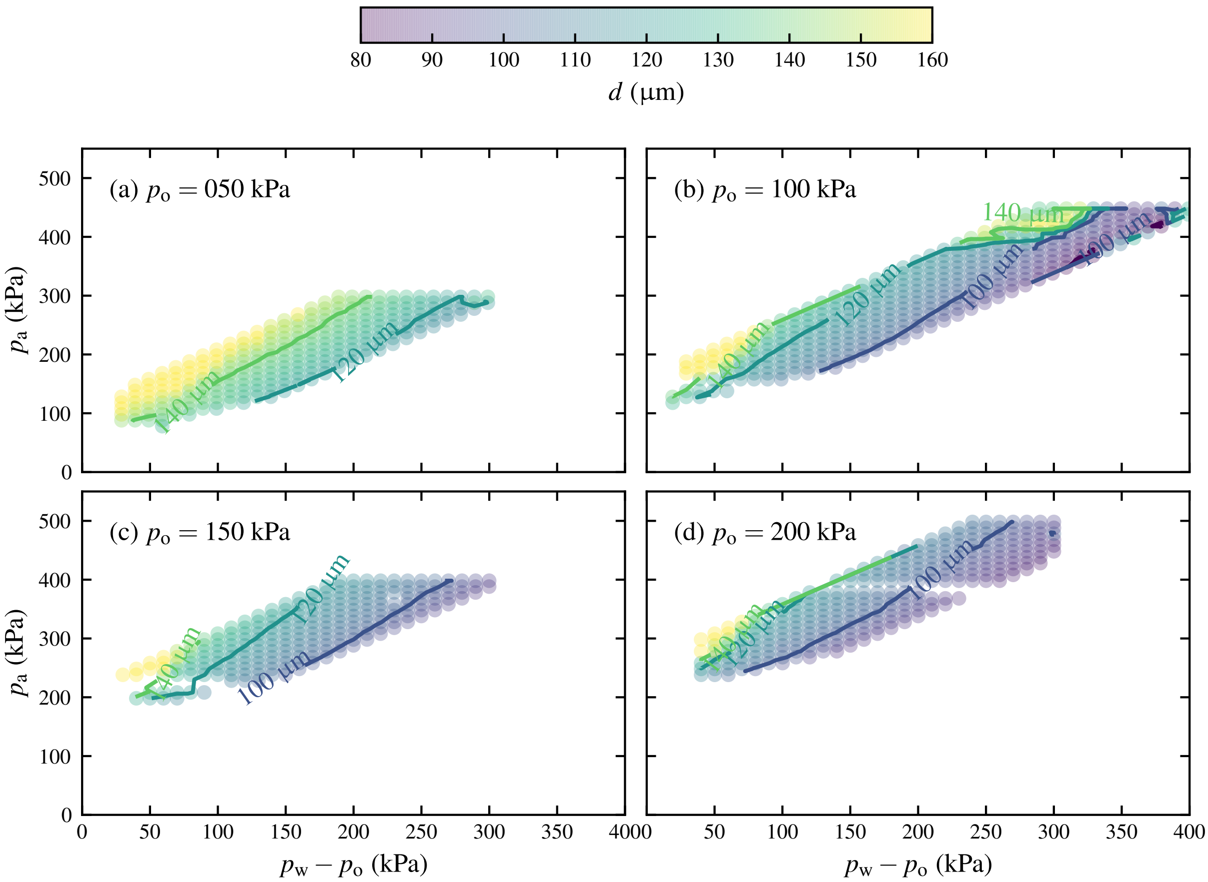

Figure 7: Diameter of generated microbubbles as a function of the driving pressure difference ($p_w - p_o$) and the air pressure (p_a), for all the investigated outlet pressure values.

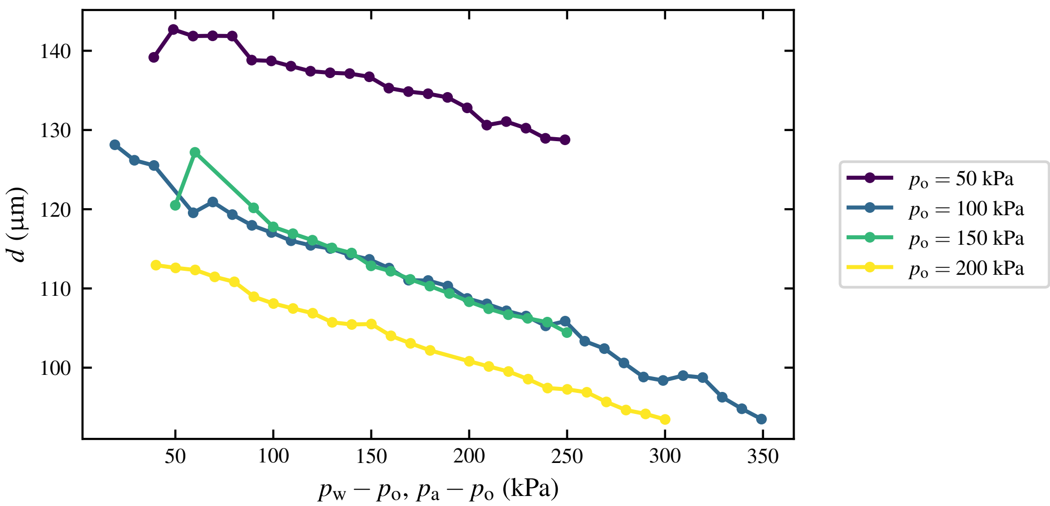

Figure 8: Microbubble diameter as a function of driving pressure difference for each outlet pressure and $p_a = p_w$.

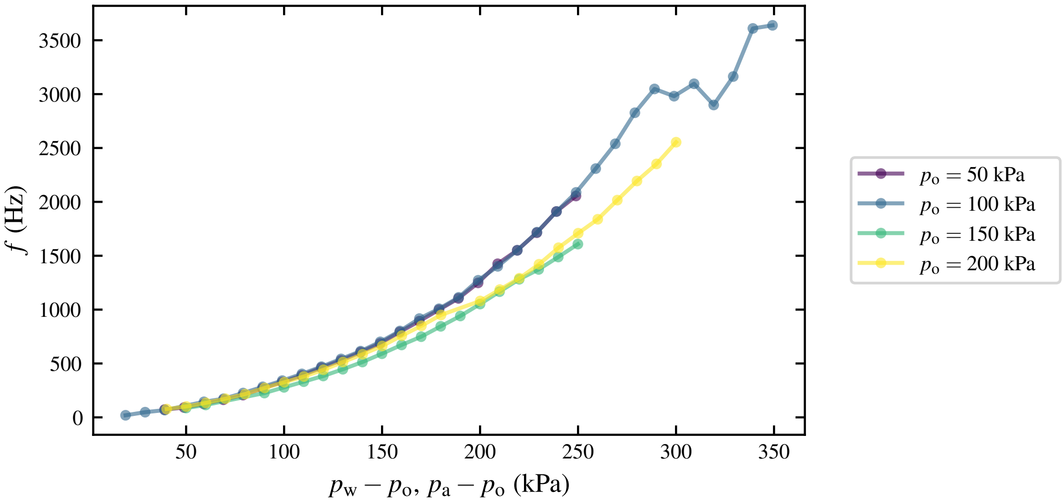

Figure 9: Bubble production rate as a function of driving pressure difference for each outlet pressure and $p_a = p_w$.

to be detrimental.

The dependence of production rate, f on $p_w - p_o$ for cases with $p_w = p_a$ across the range of investigated p_o is presented in figure 9. A quadratic increase in f with increase in $p_w - p_o$ can be observed for all p_o values. An increase in production rate, for a constant driving pressure, can be observed for lower p_o and it may be linked with an increase in $\dot{q}_a$. Note again that the data are not monotonic between the outlet pressures.

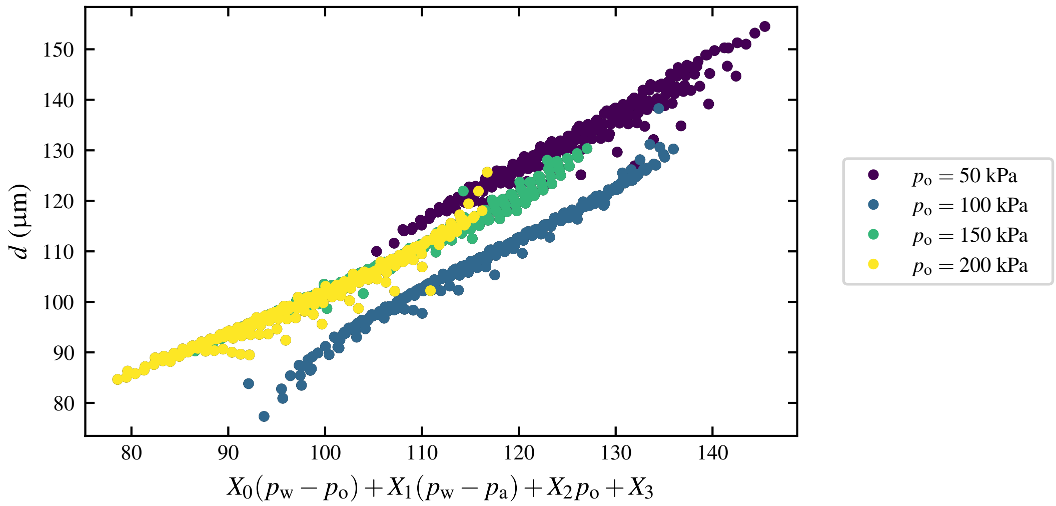

Figure 10: Empirical data fit for all pressure combinations where monodisperse bubble train was generated. X = [-0.09, -0.19, -0.15, 147.5].

Based on all the acquired data depicting the bubble diameter dependence on the input variables (p_w, p_a and p_o) an empirical scaling law is developed. The scaling law is a fit with least-squares regression to all the data where monodisperse generation was observed and it assumes the following form:

$$d = X_0(p_w - p_o) + X_1(p_w - p_a) + X_2 p_o + X_3. \tag{1}$$

The scaling function includes the main variables in form of pressure differentials used above, i.e. $p_w - p_o$ and $p_w - p_a$, as well as the absolute value of the outlet pressure. A coefficient matrix $X = [-0.09 \ -0.19 \ -0.15 \ 147.5]$ provides a reasonable fit ($R^2 = 0.86$) to all the data as it can be seen in figure 10.

4 Conclusions

Microbubble generation from a microfluidic T-junction device has been characterised across a wide range of operating conditions. The generator was observed to produce a train of monodisperse bubbles for the majority of conditions, with the exception being cases with a large difference between water and air supply pressures. The mean bubble diameter was in the range $d \approx 90 - 130$ µm. For the practical purpose of providing nucleation sites for cavitation, the change in bubble size across the observed range has a negligible effect on cavitation susceptibility, which renders the T-junction device a robust option for seeding of hydrodynamic facilities with monodisperse bubbles. Microbubble production rates of the order O(1 Hz) - O(1 kHz) have been observed, and a good control of the production rate has been demonstrated irrespective of the pressure at the device outlet. Current work provides a detailed map of the operational capabilities of a T-junction microbubble generator and adds to the ability to model nucleation effects in hydrodynamic facilities.

5 Acknowledgements

The authors wish to acknowledge the assistance of Mr Robert Wrigley and Mr Steven Kent in carrying out the experiments. The authors wish to acknowledge the support of Australian Defence Science and Technology Group within the framework of the University of Tasmania collaborative work on Office of Naval Research 2017 US Multidisciplinary University Research Initiative (MURI) titled 'Predicting turbulent multi-phase flows with high-fidelity: a physics-based approach'.

References

[1] Barbaca, L., Russell, P.S., Pearce, B.W. and Brandner, P.A. 2020, Characterization of microbubble generation in a confined turbulent jet, *Proceedings of the 22nd Australasian Fluid Mechanics Conference*

[2] Brandner, P.A., Venning, J.A. and Pearce, B.W. 2022, Nucleation effects on cavitation about a sphere, *Journal of Fluid Mechanics*, 946

[3] Khoo, M.T., Venning, J.A., Pearce, B.W. and Brandner, P.A. 2021, Nucleation and cavitation number effects on tip vortex cavitation dynamics and noise, *Experiments in Fluids*, 62(10)

[4] Rodriguez-Rodriguez, J., Sevilla, A., Martinez-Bazan, C. and Gordillo, J.M. 2015, Generation of microbubbles with applications to industry and medicine, *Annual Review of Fluid Mechanics*, 47(1)

[5] Russell, P.S., Venning, J.A., Brandner, P.A., Pearce, B.W., Giosio, D.R. and Ceccio, S.L. 2018a, Microbubble disperse flow about a lifting surface, *Proceedings of the 32nd Symposium on Naval Hydrodynamics*

[6] Russell, P.S., Giosio, D.R., Venning, J.A., Pearce, B.W., Brandner, P.A., Aumelas, V. and Maj, G. 2018b, Towards real-time optical measurement of microbubble content in hydrodynamic test facilities, *Proceedings of the 10th International Symposium on Cavitation*

[7] Scott, D.W. 2015, Multivariate density estimation: theory, practice and visualisation. John Wiley and Sons

[8] Venning, J.A., Pearce, B.W. and Brandner, P.A. 2022, The influence of nucleation on cloud cavitation about a hydrofoil, *Journal of Fluid Mechanics*, 946